ADVANCED BIOLOGY
www.advanced-bio.com

Extrusion-Based 3D Bioprinting of Adhesive Tissue Engineering Scaffolds Using Hybrid Functionalized Hydrogel Bioinks

*Shuai Chen, Martin L. Tomov, Liqun Ning, Carmen J. Gil, Boeun Hwang, Holly Bauser-Heaton, Haifeng Chen, and Vahid Serpooshan**

Adhesive tissue engineering scaffolds (ATESs) have emerged as an innovative alternative means, replacing sutures and bioglues, to secure the implants onto target tissues. Relying on their intrinsic tissue adhesion characteristics, ATES systems enable minimally invasive delivery of various scaffolds. This study investigates development of the first class of 3D bioprinted ATES constructs using functionalized hydrogel bioinks. Two ATES delivery strategies, in situ printing onto the adherend versus printing and then transferring to the target surface, are tested using two bioprinting methods, embedded versus air printing. Dopamine-modified methacrylated hyaluronic acid (HAMA-Dopa) and gelatin methacrylate (GelMA) are used as the main bioink components, enabling fabrication of scaffolds with enhanced adhesion and crosslinking properties. Results demonstrate that dopamine modification improved adhesive properties of the HAMA-Dopa/GelMA constructs under various loading conditions, while maintaining their structural fidelity, stability, mechanical properties, and biocompatibility. While directly printing onto the adherend yields superior adhesive strength, embedded printing followed by transfer to the target tissue demonstrates greater potential for translational applications. Together, these results demonstrate the potential of bioprinted ATESs as off-the-shelf medical devices for diverse biomedical applications.

1. Introduction

Traditionally, tissue engineering scaffolds are fixed onto the surface of the tissues through sutures or bioglues. Commonly used bioglues are cyanoacrylate, fibrin glue, and polyethylene glycol (PEG).[1,2] Cyanoacrylate typically suffers from relatively low biocompatibility, improper mechanical properties, and the risk of inflammation due to the toxic degradation products.[3] Fibrin glue might cause infection and has relatively low adhesion properties.[4] PEG polymers often face improper degradation and swelling characteristics.[5–8] Further, the use of sutures to secure the scaffolds on tissue could cause secondary severe damage to already fragile tissue. Adhesive tissue engineering scaffolds (ATESs) can help avoid these issues by the intrinsic adhesive properties and proper biocompatibility that supports cell viability and proliferation, implant engraftment, and tissue regeneration/repair.[9–11] ATESs can also be deployed/delivered to narrow or spatially complex/constricted areas of diseased tissue, where the use of suture or bioglue is not feasible or practical.[12] The use of adhesive hydrogels has been also explored for the repair of cardiac and vascular wounds and bleeding.[13] Another important advantage of ATES devices, in comparison to non-adhesive implants, is their ability for minimally invasive delivery, through conduits or syringes, to the surface of organs/tissues that could help to avoid aggressive

S. Chen, M. L. Tomov, L. Ning, C. J. Gil, B. Hwang, H. Bauser-Heaton, V. Serpooshan
Department of Biomedical Engineering
Emory University School of Medicine and Georgia Institute of Technology
Atlanta, GA 30322, USA
E-mail: vahid.serpooshan@emory.edu

S. Chen, H. Chen
Department of Biomedical Engineering
College of Future Technology
Peking University
Beijing 100871, China

The ORCID identification number(s) for the author(s) of this article can be found under https://doi.org/10.1002/adbi.202300124

DOI: 10.1002/adbi.202300124

L. Ning
Department of Mechanical Engineering
Cleveland State University
Cleveland, OH 44115, USA

H. Bauser-Heaton, V. Serpooshan
Department of Pediatrics
Emory University School of Medicine
Atlanta, GA 30322, USA

H. Bauser-Heaton, V. Serpooshan
Children's Healthcare of Atlanta
Atlanta, GA 30322, USA

H. Bauser-Heaton
Sibley Heart Center at Children's Healthcare of Atlanta
Atlanta, GA 30322, USA

surgeries, such as thoracotomy surgeries.[14] While the significance of ATESs in a variety of biomedical applications has been established, yet, there has been no report on the creation of more complex adhesive scaffold designs using advanced biomanufacturing modalities such as 3D bioprinting.

3D bioprinting is an additive biomanufacturing method that enables fabrication of biological constructs based on a predesigned digital model.[15–17] Traditionally, the most commonly used 3D bioprinting techniques for scaffold fabrication include extrusion-based, inkjet, and laser-based (e.g., stereolithography) bioprinting.[18] Among these techniques, micro-extrusion bioprinting has been the most common method to fabricate scaffolds through squeezing out bioinks from a syringe nozzle onto the stage in a strand-by-strand manner.[19] This printing modality offers the ability to print at high cell densities, controllable cellular damages, and less complex and cost-effective processes.[20–22] Conventional extrusion systems, however, face relatively low printing speed, inferior printing fidelity, and the limited choice of extrudable bioinks.[20] To address some of these limitations, embedded (or freeform reversible embedding of suspended hydrogels (FRESH)) bioprinting methods have been recently developed.[23–25] In the embedded extrusion approach, the bioink is deposited within a support bath that provides mechanical support to the soft ink prior to curing.[26] This unique feature enables high-fidelity extrusion-based bioprinting of a wide variety of inks, especially soft extracellular matrix (ECM)-based hydrogels that would not be printable otherwise.[25]

In this study, we utilized both the conventional and the embedded extrusion-based bioprinting methods, for the first time, to fabricate ATES solutions using a combination of methacrylated hyaluronic acid (HAMA) and gelatin methacrylate (GelMA)-based bioinks. Dopamine groups were introduced to the bioink by conjugation to the backbone of HAMA to increase the adhesion property of ATES by forming chelation with functional groups, such as amine groups or hydroxyl groups.[27] The ability of the two techniques in creating adhesive scaffolds were evaluated and compared through quantification of adhesion and mechanical properties under tensile and shear stress conditions in both static and dynamic settings. Further, swelling behavior, biocompatibility, and printing fidelity of various modalities were analyzed.

2. Experimental Section

2.1. Materials

Hyaluronic acid (HA) was purchased from Acros Organics. Gelatin, 1-(3-Dimethylaminopropyl)-3-ethylcarbodiimide hydrochloride (EDC), *N*-Hydroxy succinimide (NHS), and dopamine hydrochloride 2-Hydroxy-4′-(2-hydroxyethoxy)-2-methylpropiophenone (Irgacure 2959) were purchased from Sigma. Carbopol was purchased from Lubrizol. Dry aging collagen sheets were purchased from the Sausage Maker, USA (derived from the hide of cattle).

2.2. HAMA Bioink Preparation

HAMA preparation was conducted using a modification of a published protocol.[28] Briefly, HA was dissolved in phosphate buffered saline (PBS) solution at 0.01 g mL^{-1} concentration. Next, 5× concentration of methacrylic anhydride (MA) was added to the solution in a dropwise manner at 4 °C. 5 M NaOH was added continuously to maintain the pH of the system around 8–11. Once the entire amount of MA was added to the system, the solution was transferred to the fridge and maintained at 4 °C for 24 h. Pure ethanol was pre-cooled to 4 °C and the whole system was precipitated to the pre-cooled ethanol (volume of ethanol:volume of the solution = 5:1) under vigorous stirring and the white precipitation was collected by centrifuge. The process was repeated three times. The collected HAMA was dialyzed against distilled water for three days, freeze dried, and kept at 4 °C until use.

2.3. Preparation of Dopamine Modified HAMA (HAMA-Dopa)

Grafting of dopamine onto the backbone of HAMA and preparation of HAMA-Dopa were performed following a modification of a published protocol.[12] Briefly, HAMA was dissolved in an aqueous solution at a 0.01 g mL^{-1} concentration. Subsequently, 7.2 mg mL^{-1} of EDC and 4.3 mg mL^{-1} of NHS were added to the solution and stirred for 30 min (the molar ratio of EDC/NHS to HAMA monomers was 1.5:1). Next, 7.1 mg mL^{-1} of dopamine hydrochloride was added to the solution and the reaction was maintained for 10 h at the pH of 4–5 (molar ratio of dopamine to HAMA monomers was maintained at 1.5:1). After reaction, the system was dialyzed against distilled water for three days and freeze dried to obtain the HAMA-Dopa foam.

2.4. GelMA Preparation

GelMA preparation was conducted based on a published protocol with some modifications.[29] Briefly, 20 g porcine gelatin (Sigma) was dissolved in PBS solution at a 0.1 g mL^{-1} concentration. Next, 2 g of MA was added to the solution in a dropwise manner at 50 °C. 5 M NaOH was added to the solution continuously to keep the pH of the solution around 8–11. After 2.5 h, the reaction was quenched by the addition of HCl to alter the pH value of the system to around 7. Then, 2× of PBS solution, preheated to 50 °C, was added to the system and the solution was injected through 0.25 μm syringe filters to remove the precipitate. The solution was next dialyzed against water for 3 days and then freeze-dried.

2.5. ^{1}H NMR Spectroscopy

^{1}H NMR spectroscopy was performed using a 500 MHz spectrometer (Bruker, US) (**Figure 1**C). The synthesized HAMA, HAMA-Dopa, and GelMA were dissolved in deuterium oxide (99.9%) at the concentration of 5 mg mL^{-1}. The solution was next lyophilized and the obtained products were re-dissolved in deuterium oxide. The process was repeated twice to remove the hydrogen oxide molecules from the product and reduce the height of the peak from hydrogen oxide. Finally, the products were dissolved in deuterium oxide at the concentration of 5 mg mL^{-1} and the solutions were transferred to NMR tubes to perform the ^{1}H NMR spectroscopy.

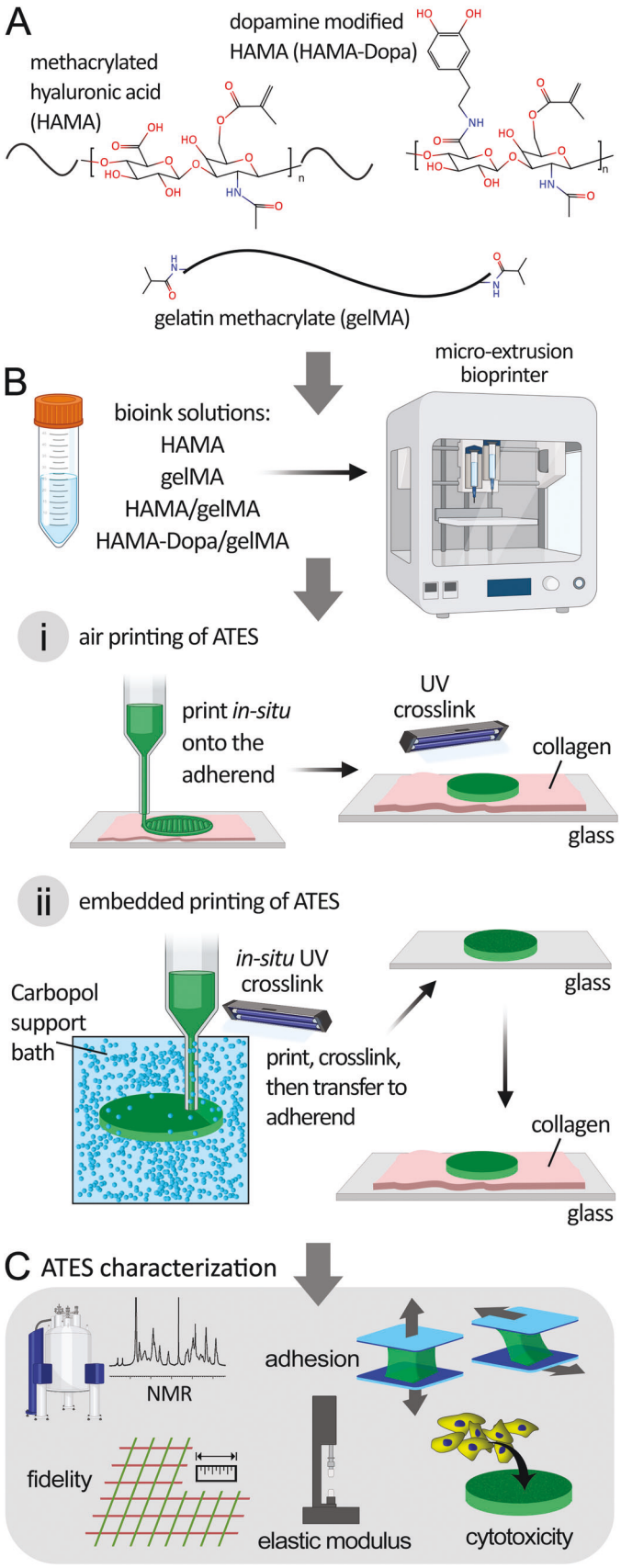

Table 1. Experimental conditions used for 3D bioprinting of ATES systems.

Ingredient	Concentration [wt%]	Crosslinking intensity [mW cm^{-2}]	Crosslinking time [s]	Printing method
HAMA	1%	20	120	Embedded
GelMA	10%	20	120	Embedded
HAMA/GelMA	1%/10%	20	120	Embedded
HAMA-Dopa/GelMA	1%/10%	20	120	Embedded
HAMA-Dopa/GelMA	1%/10%	20	30	Air printing

2.6. Bioprinting Processes to Create ATES Systems

Carbopol particles (0.8 wt/v%) were added to distilled water and stirred for 24 h. Subsequently, the pH was adjusted at 7 which turned the mixture into a semi-solid state used as the support bath. Four groups of bioinks were prepared and used to print various ATES systems in this study (**Table 1**, Figure 1A). For each bioink group, 0.5% of Irgacure was used as the photoinitiator. The bioinks were loaded on a syringe and printed using a BIO X micro-extrusion bioprinter (CELLINK) based on models designed by CAD software. Two methods of bioprinting, that is, air bioprinting and embedded bioprinting, were used (Figure 1B-i,ii). In the air printing method, the bioinks were directly printed onto the substrate, that is, the surface of the collagen sheet, and then crosslinked in situ by the UV light (380 nm).[30] In the embedded printing approach, the bioinks were extruded into a Carbopol support bath and cured using the UV light.[23,31] Crosslinking parameters were tuned for each bioink solution to achieve optimized mechanical and fidelity properties (Table 1). In the embedded printing method, the temperature was set at 30 °C in the support bath, 38 °C for the syringes containing the HAMA, HAMA/GelMA, and HAMA-dopa/GelMA bioinks, and 30 °C for the GelMA bioink. In the air printing method, the temperature was set at 19 °C for the substrate and 24 °C for the syringe containing the bioink. In the embedded printing, the pressure was set at 40 kPa for the HAMA and HAMA/GelMA groups, 80 kPa for the HAMA-dopa/GelMA group, and 20 kPa for the GelMA group. In the air printing method, the pressure was set at 120 kPa.

Following the embedded bioprinting, ATESs were harvested from the support bath by the addition of PBS solution and rinsed with PBS (three times) to remove the residual Carbopol before use in the following experiments.

2.7. Bioprinting Fidelity Analysis

Fidelity of bioprinted ATES constructs was evaluated at two different scales as previously reported.[23,30–32] First, strand-level (micro) fidelity was examined[31] by printing a 2D network of bioink strands on the glass slide based on a lattice pattern designed by CAD software (Figure 1C). The diameter of the strands (d_{strand}), the angle between two crossing strands (α_{strands}), and the area between two pairs of parallel strands (A_{strands}) were measured (ImageJ) and normalized by dividing to the corresponding values in the CAD design ($d_{\text{strand in CAD}}$, $\alpha_{\text{strands in CAD}}$, and $A_{\text{strands in CAD}}$) using the following equations:

$$r_{\text{d,strand}} = \frac{d_{\text{strand in print}}}{d_{\text{strand in CAD}}} \times 100 \quad (1)$$

$$r_{\alpha,\text{strand}} = \frac{\alpha_{\text{strands in print}}}{\alpha_{\text{strands in CAD}}} \times 100 \quad (2)$$

$$r_{\text{A,strand}} = \frac{A_{\text{strands in print}}}{A_{\text{strands in CAD}}} \times 100 \quad (3)$$

The ratios $r_{\text{d,strand}}$, $r_{\alpha,\text{strand}}$, and $r_{\text{A,strand}}$ were plotted for each bioink formulation to represent their strand/micro fidelity for bioprinting.

Further, the bulk (macro) scale fidelity was measured after printing the ATES constructs. For this purpose, the diameter, perimeter, and cross-sectional area of printed scaffolds were measured (ImageJ) and divided by the corresponding theoretical values, in the CAD file, using the following equations:

$$r_{\text{d,bulk}} = \frac{d_{\text{ATES in print}}}{d_{\text{ATES in CAD}}} \times 100 \quad (4)$$

$$r_{\text{P,bulk}} = \frac{P_{\text{ATES in print}}}{P_{\text{ATES in CAD}}} \times 100 \quad (5)$$

$$r_{\text{A,bulk}} = \frac{A_{\text{TES in print}}}{A_{\text{ATES in CAD}}} \times 100 \quad (6)$$

The ratios $r_{\text{d,bulk}}$, $r_{\text{P,bulk}}$, and $r_{\text{A,bulk}}$ were plotted for all bioink formulations, representing their bulk fidelity for bioprinted ATES constructs.

Finally, ATES constructs made using HAMA-Dopa/GelMA bioink, and using embedded and air bioprinting methods, were immersed in PBS for 7 days and then harvested for fidelity assessments. The diameter, perimeter, and area of scaffold samples were measured and the ratios were calculated by dividing each parameter on day 7 to that on day 0 (pre-incubation in PBS), using the following equations:

$$r_{\text{d,day 7}} = \frac{d_{\text{ATES at day 7}}}{d_{\text{ATESat day 0}}} \times 100 \quad (7)$$

Figure 1. The workflow used in this study to fabricate and characterize adhesive tissue engineering scaffold (ATES) systems. A) Various bioink formulations were prepared using methacrylated hyaluronic acid (HAMA), dopamine modified HAMA (HAMA-Dopa), and gelatin methacrylate (GelMA). B) Hybrid bioinks were 3D bioprinted (micro-extruded) either directly onto the adherend collagen substrate (air printing, i), or embedded bioprinted within a Carbopol support bath (ii), harvested by PBS wash, and transferred onto the recipient surface (collagen sheet on a glass slide substrate). For both methods, fabricated ATESs were crosslinked by UV light, either post-print (air method) or in situ in the embedding bath. C) Characterization of bioprinted ATESs was performed using a variety of techniques, including nuclear magnetic resonance (NMR) spectroscopy, adhesive strength measurements, printing fidelity analysis, microindentation, and cell viability and growth assays.

$$r_{P,\text{day }7} = \frac{P_{\text{ATES at day }7}}{P_{\text{ATES at day }0}} \times 100 \quad (8)$$

$$r_{A,\text{day }7} = \frac{A_{\text{ATES at day }7}}{A_{\text{ATES at day }0}} \times 100 \quad (9)$$

The ratios $r_{d,\text{day }7}$, $r_{P,\text{day }7}$, and $r_{A,\text{day }7}$ therefore represented a combination of bulk fidelity and swelling/degradation of ATESs at day 7.

2.8. Evaluation of Adhesion Properties ATESs

Customized experimental set-ups were developed to measure the adhesion properties of ATESs under shear and tensile stresses (Figure 1C). A piece of thin, dry collagen sheet was used as the adhesion substrate imitating the native tissue. The ATES was adhered onto the collagen sheet from one side, which imitated the tissue surface, and the other side of ATES was glued to the glass slide (with no effect on the interface with collagen). The assembly was sandwiched between two glass slides. A 50-mL Falcon tube was hung underneath the assembly, hence, applying a pure tensile stress to the adhered scaffold. Water drops were injected into the tube in a steady manner, using a peristaltic pump, to apply incremental tensile stress. The stress at the breaking point of the ATES adhesion to the collagen sheet was measured (weight of the water + tube).

To measure adhesive strength under shear loading, the ATES was sandwiched between a collagen sheet attached to a glass slide, on one side, and another glass slide glued onto the other side of ATES (as above). Drop-wise continuous injection of water into a balloon was used to apply perpendicular force to the adhesion interface. Increasing shear was applied to the samples, via a peristaltic pump, until the connection between the collagen sheet and the ATES was broken. For both tensile and shear assays, the adhesive strength was measured using the following equation:

$$\text{Adhesion strength} = \text{stress}_{\max} = \frac{\text{weight}_{\max}}{\text{adhesion area}} \quad (10)$$

To imitate the in vivo conditions for a cardiac patch, adhered onto the epicardial surface under dynamic loading and immersed in fluid, a beating silicon balloon platform was set up. The contractile balloon models underwent inflation–deflation cycles (of air) at a 60 beat per minute (BPM) rate (recapitulating that of the adult human heart[33]) using a programmed bioreactor (Ibidi, USA).[34] For this purpose, the ATES was adhered to the collagen sheet (no glue), and then the assembly was glued to the surface of the silicon balloon. The whole system was immersed into deionized (DI) water. The cyclic loading was performed for a maximum 4 days and the number of cycles that each ATES could tolerate before breaking the interface was recorded, to represent the dynamic wet adhesive strength.

2.9. Mechanical Characterization of ATES Constructs

Elastic modulus (E) of ATES constructs was measured via a compression test, using a mechanical testing system (Shimadzu, Japan). The test device was mounted with a circular column probe and the ATESs were loaded onto the machine. The heights of the ATESs were measured by descending the probe until it contacted the upper surface of the scaffold sample. The compressive force was applied to the samples steadily at a 1 mm s^{-1} rate until the probe reached the 5 N limit. Load–displacement data were recorded. The stress–strain data were subsequently calculated by dividing load and displacement by cross-sectional area (constant) and the initial height of ATEM samples, respectively. The Young's (elastic) modulus (E) was calculated at the 10% displacement point.

2.10. Swelling Behavior of the ATES Constructs

Scaffolds were immersed in PBS solution their weight was measured (W_t) at days 0, 3, and 7. The swelling of the ATES was calculated using the following equation:

$$\text{Swelling ratio} = \frac{W_t}{W_{t=0}} \quad (11)$$

where $W_{t=0}$ is the weight of the sample at the beginning of the assay.

2.11. Cytotoxicity of ATES Constructs

For the Live/Dead assay, ATESs were sterilized by UV light for 1 h and were immersed in the culture media for mouse fibroblast (L929) cells overnight. Subsequently, L929 fibroblasts were seeded onto the ATESs (5×10^5 cells mL^{-1}) and 1 mL of fresh culture media was added to each well. At different time points during culture, the ATESs were stained with Live/Dead fluorescent dye (1 µL LiveDye and 1 µL NucleiDye (Abbkine, China) in 1 mL 1× PBS) and imaged using an epifluorescence microscope.[35,36]

Cell Counting Kit-8 (CCK-8) test was used to assess cytotoxicity of bioprinted ATES samples.[37] For this purpose, the media incubated with ATESs were collected and used to culture mouse fibroblast (L929) cells (Procell, China). Bioprinted scaffolds were sterilized under the UV light for 1 h and then were immersed overnight in the complete L929 medium (at the weight ratio of 0.1 ATES:medium) to obtain the ATES-extracted media. L929 cells were seeded in a 96-well plate at a density of 3×10^5 cells/well. Subsequently, 100 µL of complete L929 medium was added to each well and the cells were cultured at 37 °C overnight. The next day, the media was discarded and the same amount of ATES-extracted media was added to each well. At multiple time points, the extracted media was removed, the complete medium with 10% of CCK-8 reagent (Yeason, China) was added to each well, and the plate was incubated at 37 °C for 1 h. Subsequently, the optical density (OD) at 450 nm was measured using a multifunction microplate reader (SpectraMax, China). Four replicates (n = 4) were made for each measurement. The group cultured by pure medium was used as control. The cytotoxicity of ATESs was represented by the ratio of absorbance of experimental groups (with extracted media) to that of the control group (pure culture media).[38,39]

2.12. Statistical Analysis

Experimental data were processed and expressed using mean values ± standard deviation (SD). Statistical significance was determined by *t* test, one-way or two-way analysis of variance, and multiple comparisons were performed and corrected by Tukey test using GraphPad Prism with an acceptable significance level of $p < 0.05$. In the entire study, *: $p < 0.05$, **: $p < 0.01$, and ***: $p < 0.001$ in comparison to the defined control/reference groups.

3. Results and Discussion

Tissue engineered scaffolds are typically implanted onto the target tissue (i.e., injury site) using various suture and bioglue techniques.[7,14] There are several challenges that limit the application of these techniques, including cytotoxic effects and secondary damages, poor adhesive or degradation properties, and possible infection or allergic/immune responses.[40–42] ATES systems have recently emerged as an alternative means to address these limitations by providing intrinsic tissue adhesion functionality.[14,43] Traditionally, ATESs have been applied to the target tissue either through direct injection/casting of the pre-hydrogel solution,[29,44–46] or via adhesion of the solidified scaffold in the form of foams,[47] cast hydrogels,[48] or electrospun patches.[49] These conventional ATES systems, however, lack complex structural and functional features required in the personalized and precision medicine paradigms to repair/regenerate tissues and organs. There has been no report on adoption of 3D bioprinting technologies to manufacture hydrogel-based ATES constructs. This work introduces the first generation of such systems. Compared to conventional scaffold fabrication methods, bioprinting enables creation of complex structural/functional designs, including both internal and external features such as vascular networks,[50] heterogenous pattering of cells and/or small molecules,[51] and patient-specific scaffold shape/geometry.[30,52] The integration of intrinsic and enhanced adhesive properties, together with complex structural/functional features in bioprinted ATES systems can provide robust implant solutions for a variety of regenerative medicine applications.

In the presented study, a new manufacturing paradigm is established to create functional, customized ATES constructs for a variety of biomedical applications. Conventional extrusion-based bioprinting (in the air), together with the embedded bioprinting approach, were used for the first time to create hydrogel-based ATES devices with highly tunable physiomechanical and biological functions (Figure 1).

To date, various hydrogel biomaterials have been used to engineer ATES systems, including peptide-conjugated chitosan hydrogel scaffolds,[53] alginate and alginate-gelatin based hydrogels,[54] the horseradish peroxidase-catalyzed hydrogel,[55] and other polymer-based bioadhesives.[56] There is, however, no report on the use of hydrogel-based bioinks for 3D bioprinting of such self-adhesive tissue engineering scaffolds.[57] Among various hydrogel solutions used to date in extrusion bioprinting processes, HAMA and GelMA are among the most commonly used bioinks.[58–60] These functionalized hydrogels consist of HA and gelatin, which are key ECM components of many tissues and organs.[61–63] To generate HAMA bioinks in this study, the methacrylate groups were modified onto the backbone of the HA through the reaction of MA with hydroxyl groups of HA. Successful synthesis of HAMA was confirmed via ^{1}H NMR spectroscopy which demonstrated the peaks at 1.9 ppm and 5.6-6.1 ppm, representing the N-acetyl glucosamine of HA and the methacrylate protons, respectively (**Figure 2**A-i,ii).[28] The degree of modification of methacrylate to the backbone of HA ($D_{\text{MA-HA}}$) was calculated to be 31.25%, based on the areas under the peaks at 1.9 ppm (Area_{i}) and 5.6–6.1 ppm (Area_{ii}) (Figure 2A), using the following equation:

$$D_{\text{MA-HA}} = \frac{3 \times \text{Area}_{\text{ii}}}{2 \times \text{Area}_{\text{i}}} \times 100 \quad (12)$$

The dopamine groups were modified into the backbone of HAMA through the amidation reaction between the amino group of the dopamine hydrochloride and the carboxyl group of the HAMA. The NMR results showed a peak at 6.85–7.31 ppm, corresponding to the protons from the benzene ring, hence, confirming the successful dopamine modification of HAMA (Figure 2A-iii).[12,64] The degree of dopamine modification of HAMA ($D_{\text{Dopa-HAMA}}$) was calculated at 23.04% from the area under the peak at 6.85–7.31 ppm (Area_{iii}) and the peak at 1.9 ppm (Area_{iv}), using the following equation:

$$D_{\text{Dopa-HAMA}} = \frac{\text{Area}_{\text{iii}}}{\text{Area}_{\text{iv}}} \times 100 \quad (13)$$

Incorporation of methacrylate groups into the backbone of gelatin was through the reaction of MA and amino groups from the backbone of gelatin. The NMR peak at 2.8–2.95 ppm represented the lysine methylene protons of the unreacted lysine group on the backbone of gelatin (Figure 2B-i). The peaks at 5.2–5.7 ppm represented the acrylic protons of methacrylate groups modified onto the backbone of gelatin (Figure 2B-ii).[65,66] The degree of methacrylation of gelatin ($D_{\text{MA-gelatin}}$) was calculated at 91.74%, based on the areas under the peak of 2.8–2.95 ppm (Area_{i}) and 5.2–5.7 ppm (Area_{ii}), using the following equation:

$$D_{\text{MA-gelatin}} = \frac{\text{Area}_{\text{ii}}}{\text{Area}_{\text{i}}+\text{Area}_{\text{ii}}} \times 100 \quad (14)$$

Together the NMR results confirmed the successful functionalization of both HA and gelatin with MA, and further modification of HAMA with dopamine, to create HAMA-Dopa hydrogel, used in this study as the base of bioinks. The MA groups modified to the backbone of HA and gelatin enable UV-initiated generation of free radicals. These radicals can, in turn, react with the moieties on the surface of the substrate during the bioprinting step to improve adhesion properties, and also react with each other to crosslink the bioink polymer post printing. Dopamine groups modified to the backbone of HAMA can further enable formation of chelation with functional groups on the surface of the substrate to improve the adhesive properties of bioprinted ATES.

Prepared HAMA and GelMA-based bioink solutions were subsequently used to bioprint ATES constructs. First, we examined the printability of various bioinks using our well-established macro (bulk)- and micro (strand)- level fidelity measurement protocols (**Figure 3**, **Table 2**).[31,32,67] The bulk

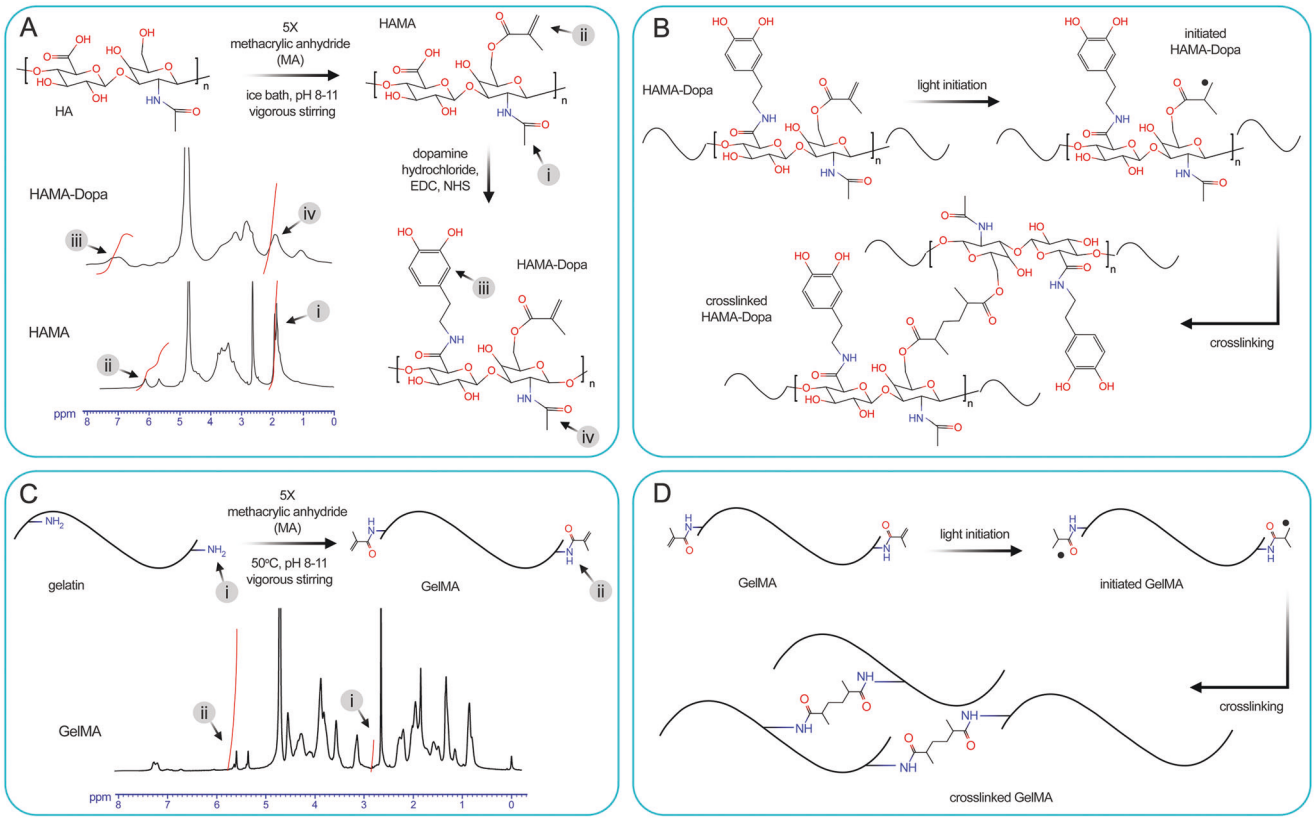

Figure 2. Preparation and nuclear magnetic resonance (NMR) spectroscopy analysis of hydrogel bioinks used in this study. A) Preparation and NMR spectra of methacrylated hyaluronic acid (HAMA) and dopamine-modified HAMA (HAMA-Dopa). Protons from the *N*-acetyl glucosamine of HA (i, iv), from the methacrylate of methacrylic anhydride (MA) groups (ii), and from the benzene ring of dopamine group (iii) are highlighted. B) Initiation and crosslinking of HAMA-Dopa under the UV light. C) Preparation and NMR spectrum of gelatin methacrylate (GelMA). Protons from the unreacted lysine methylene of GelMA (i) and from the methacrylate groups modified onto the backbone of gelatin (ii) are highlighted. D) Crosslink process of GelMA under the UV light.

fidelity measurements of ATES diameter (d) showed $r_{d,bulk}$ ratios 78 ± 1%, 92 ± 1%, 87 ± 1%, 88 ± 1%, and 93 ± 1% for HAMA, GelMA, HAMA/GelMA, HAMA-Dopa/GelMA (embedded printed), and HAMA-Dopa/GelMA (air printed) groups, respectively (Figure 3A,B, Table 2). Further, the perimeter of disc-shape constructs was measured to calculate $r_{P,bulk}$ ratios of 81 ± 1%, 96 ± 1%, 91% ±1%, 95 ± 2%, and 102 ± 1% for HAMA, GelMA, HAMA/GelMA, HAMA-Dopa/GelMA (embedded printed), and HAMA-Dopa/GelMA (air printed) groups, respectively (Figure 3A,B, Table 2). Finally, we measured the cross-sectional surface areas (A) of ATESs and calculated the $r_{A,bulk}$ ratios of 60 ± 1%, 84 ± 1%, 76% ± 2%, 77 ± 2%, and 86 ± 1% for HAMA, GelMA, HAMA/GelMA, HAMA-Dopa/GelMA (embedded printed), and HAMA-Dopa/GelMA (air printed) groups, respectively (Figure 3A,B, Table 2). Of note, embedded bioprinted ATES constructs, for all four bioink groups, resulted in diameter, perimeter, and area ratios ($r_{d,bulk}$, $r_{P,bulk}$, and $r_{A,bulk}$) smaller than 100% (i.e., prints smaller than the CAD model). This may be due to the under-extrusion of bioinks, caused by the reduced flow rate of the ink due to the resistance of the support Carbopol bath, as reported before.[23,26,68] Another factor that may have contributed to the reduced print size is the possible shrinkage/deformation of constructs post printing, during the crosslinking or following steps.[69,70] Future works could benefit from precise (extrusion) flow rate measurements, as well as dimensional measurements pre and post crosslinking, to tease out the potential contributions of under/over-extrusion and shrinkage/swelling to the fidelity results. The air printed HAMA-Dopa/GelMA scaffolds, demonstrated greater $r_{d,bulk}$, $r_{P,bulk}$, and $r_{A,bulk}$ values, approaching the 100% value, in comparison to the embedded bioprints (Figure 3B). The superior fidelity of air printed constructs could confirm the effect of support bath resistance on reducing the bioink flow and hence, deteriorating the bulk fidelity of embedded bioprints.

Achieving structural stability/fidelity of bioprinted constructs following their exposure to biological milieu is an important feature that could have significant impact in their in vitro and in vivo applications. We next measured the structural stability of the embedded and air printed HAMA-Dopa/GelMA constructs following a 7-day incubation in PBS solution (Figure 3C,D, Table 2). The stability ratios $r_{d,day7}$, $r_{P,day7}$, and $r_{A,day7}$ (calculated by dividing each parameter measured at day 7 to that measured in day 0) were at 102 ± 1%, 97 ± 3%, and 104 ± 2%, respectively, for the embedded printed HAMA-dopa/GelMA group. For the air printed group, $r_{d,day7}$, $r_{P,day7}$, and $r_{A,day7}$ ratios were calculated at 98 ± 3%, 100 ± 1%, and 96 ± 5%, respectively. Overall, these

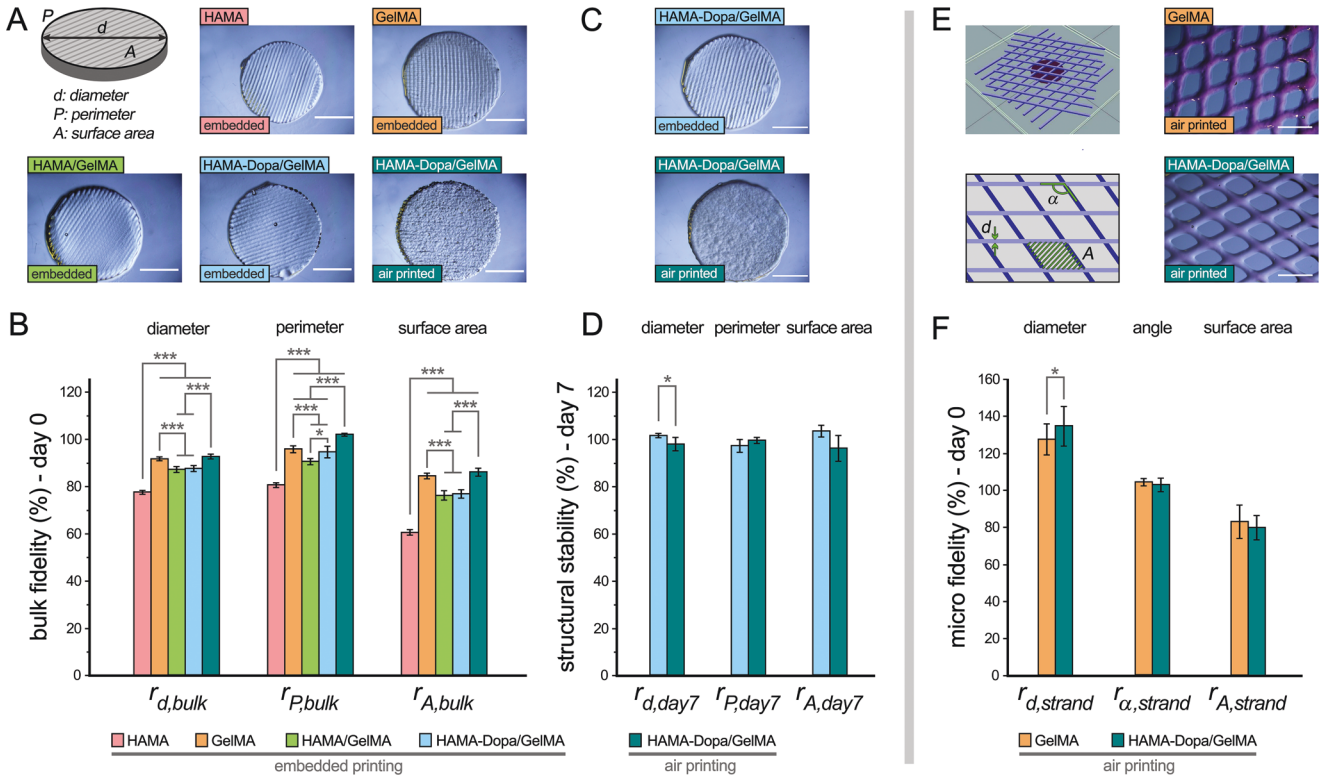

Figure 3. Evaluation of bioprintability of the bioinks developed and used in this study through measurement of macro (bulk) and micro (strand-level) fidelity and structural stability. A) Adhesive tissue engineering scaffold (ATES) constructs were printed using a disk-shape design (first panel) at the diameter (d), perimeter (P), and cross-sectional area (A). Images of printed constructs are shown for methacrylated hyaluronic acid (HAMA), gelatin methacrylate (GelMA), HAMA/GelMA, and dopamine-modified HAMA (HAMA-Dopa)/GelMA printed via embedded technique, and HAMA-Dopa/GelMA via air printing. B) Bulk fidelity of ATES constructs, obtained by measuring the diameter (d), perimeter (P), and cross-sectional area (A) of bioprints and normalizing them by the corresponding CAD values, to calculate $r_{d,bulk}$, $r_{P,bulk}$, and $r_{A,bulk}$ ratios, respectively ($n = 4$). C,D) Structural stability measurements ($r_{d,day7}$, $r_{P,day7}$, and $r_{A,day7}$) for the main study group (HAMA-Dopa/GelMA), created via embedded versus air printing techniques, after 7 days of incubation in PBS, normalized to measurements at day 0 ($n = 4$). E,F) Micro (strand-level) fidelity measurement of developed GelMA (control) and HAMA-Dopa/GelMA (main study group) bioinks were measured by printing an interwoven lattice pattern model, consisting of two sets of parallel strands. Fidelity was calculated for the strand diameter (d_{strand}), angle between two strands ($\alpha_{strands}$), and the area between strands ($A_{strands}$) by measuring the printed parameters and normalizing by the CAD values. Obtained ratios $r_{d,strand}$, $r_{\alpha,strand}$, and $r_{A,strand}$ were plotted for each group ($n = 4$). Data are represented as mean ± standard deviation. *: $p < 0.05$, **: $p < 0.01$, and ***: $p < 0.001$.

Table 2. The results of measurement of micro- and macro- fidelity and structural retention of various bioprinted constructs tested in this study.

		HAMA (emb. print)	GelMA (emb. print)	HAMA/GelMA (emb. print)	HAMA-dopa/GelMA (emb. print)	GelMA (air print)	HAMA-dopa/GelMA (air print)
Macro-fidelity (day 0)	Scaffold diameter (d, bulk)	78 ± 1%	92 ± 1%	87 ± 1%	88 ± 1%	—	93 ± 1%
	Perimeter (P, bulk)	81 ± 1%	96 ± 1%	91% ±1%	95 ± 2%	—	102 ± 1%
	Surface area (A, bulk)	60 ± 1%	84 ± 1%	76% ± 2%	77 ± 2%	—	86 ± 1%
Structural retention (day 7)	Scaffold diameter (d, day7)	—	—	—	102 ± 1%	—	98 ± 3%
	Perimeter (P, day7)	—	—	—	97 ± 3%	—	100 ± 1%
	Surface area (A, day7)	—	—	—	104 ± 2%	—	96 ± 5%
Micro-fidelity (day 0)	Strand diameter (d, strand)	—	—	—	—	128 ± 8%	135 ± 11%
	Angle between strands (α, strand)	—	—	—	—	104 ± 2%	103 ± 3%
	Area between strands (A, strand)	—	—	—	—	83 ± 9%	80 ± 6%

results suggest relatively small level of structural alterations in the bioprinted ATES constructs (≈91–106%) (Figure 3D, Table 2). The printing modality (embedded vs air printing) did not seem to have notable effect on the structural stability of the ATESs after 7 days of incubation, except for some small (but significant) difference in the construct diameter.

We subsequently examined the micro-fidelity of the main bioink solution used in this study, that is, the HAMA-Dopa/GelMA bioink, to more closely assess the printability of the ink in comparison to a GelMA control group (Figure 3E,F, Table 2). Air-printed strands showed $r_{d,strand}$ ratios (strand diameter) of 128 ± 8% and 135 ± 11% for the GelMA and HAMA-Dopa/GelMA bioinks, respectively. Further, the GelMA and HAMA-Dopa/GelMA bioinks exhibited $r_{\alpha,strand}$ ratios (angle between crossing strands) of 104 ± 2% and 103 ± 3%, respectively. And the $r_{A,strand}$ values (the area between strands) were measured at 83 ± 9% and 80 ± 6% for the GelMA and HAMA-Dopa/GelMA inks, respectively (Figure 3F, Table 2). These data indicate rather uniform printed strands for both bioink solutions, with insignificant differences ($p > 0.05$) between the two inks. The relatively large deviation of printed strand diameters, in reference to the CAD design, could be attributed to the potential swelling/shrinkage of extruded hydrogels, the surface tension properties of the bioinks, and/or the collapse/deformation caused by the gravity.[70] The angles of the printed strands were close to those in the CAD model, approaching 100%, which helped to maintain the shape of the printed lattice. The areas enclosed between the printed strands were smaller than those in the design, possibly due to the increased strand diameters and bioink melting/fusion. Overall, these data demonstrated acceptable printability of the functionalized HAMA-Dopa/GelMA bioink solution developed in this study to print ATES systems.

Following the in-depth characterization of developed bioinks and bioprinted ATES constructs, we evaluated the adhesive strength of fabricated scaffolds under varying loading conditions (**Figure 4**; Figure S1, Supporting Information). Considering the diversity of the biomedical applications for ATES systems, in both in vitro and in vivo settings, testing their inherent adhesion properties under tensile versus shear, static versus dynamic, and dry versus wet conditions would be of great importance. In all experiments, the modification of dopamine groups increased the adhesion property of HAMA-dopa/GelMA scaffolds, in comparison to non-modified groups, due to the chelation formed between the phenols and the hydroxyl and carboxyl groups of the surface of the adherend (Figure 4A–D; Figure S1, Supporting Information). Results from steadily increasing tensile stress demonstrated that the air-printed HAMA-dopa/GelMA scaffolds exhibited remarkably (an order of magnitude) higher levels of tensile adhesion strength (10.13 ± 1.14 kPa) in comparison to the embedded printed groups consisting of same bioink (0.48–1.03 kPa) ($p < 0.001$) (Figure 4A). This could be explained by the fact that in the air printing process, the bioink was extruded and cured directly on the surface of the adherend. Thus, in air-printed ATES, the radicals initiated by the UV light from the methacrylate groups could react with the hydroxyl and carboxyl groups on the surface of the substrate to increase the adhesion properties (Figure 4D). Furthermore, the bioink in air-printed groups was extruded on the surface of the collagen sheet in a semi-liquid state which possibly enhanced the penetration, integration, and (physical) entanglement of the ink within the substrate's porous surface. This is while the embedded bioprints were removed from the support bath and transferred onto the collagen sheet in a solid/cured state for the adhesion testing, resulting in limited interactions with the host and hence, lower adhesion strengths (Figure 4A,D).

Testing printed ATES systems under incremental shear loading demonstrated a similar trend to the tensile strength, with the HAMA/GelMA and HAMA-Dopa/GelMA scaffolds showing significantly higher ($p < 0.001$) shear adhesion strengths (0.55 ± 0.03 kPa) in comparison to HAMA, GelMA, and HAMA/GelMA groups (0.24 ± 0.03, 0.23 ± 0.03, 0.36 ± 0.03 kPa, respectively) (Figure 4B). This could be attributed to the significant effect of dopamine modification as explained above. The in situ air-printed HAMA-Dopa/GelMA samples did not break their adhesion to the collagen sheet under the maximum stress applicable in this custom-built experimental set-up (0.76 kPa), confirming their markedly superior adhesion properties compared to other (pre-printed) ATES groups. The limitation in max shear stress applied is considered as a technical limitation of the custom-built set-up for these tests that can be addressed in future works. It should be noted that for all adhesive strength tests, the ATES side that was glued to the glass slide maintained the applied forces and the samples break/rupture only occurred at their interface with the collagen sheet (no glue, self-adhesion effect). Therefore, the measured forces are indicative of the self-adhesion property of each scaffold group. While the air printed scaffolds showed superior adhesive characteristics, comparing to the embedded printed ones, they strictly require an in situ bioprinting and crosslinking process to achieve the desired adhesive properties. This largely limits the applications of air-printed ATESs, particularly for the in vivo/clinical applications. Therefore, for the rest of this study, we mainly focused on the embedded bioprinted ATES constructs which offer the potential for mass manufacturing and off-the-shelf presentation for a wide variety of biomedical applications.

While various multifunctional adhesive scaffolding systems have been developed, in most cases, their therapeutic efficacy for tissue repair has been limited due to their inadequate adhesive properties in the physiological environment, that is, in dynamic wet/underwater loading conditions.[14,71,72] To further recapitulate the loading conditions in the in vivo applications, we tested the adhesion strength of ATES groups under dynamic (cyclic) loading, using a beating heart model that was submerged in the water (Figure 4C; Figure S1C, Supporting Information). The apparatus closely recapitulated the beating pattern of adult human heart (60 BPM[33]) and demonstrated a markedly higher ($p < 0.001$) adhesion property of the air-printed ATESs, which remained on the beating balloon under water for up to 4 days (345 600 cycles) (Figure 4C-ii). This is while the embedded printed HAMA-Dopa/GelMA group could tolerate this harsh loading scenario only for several minutes (383 cycles). Maintaining proper adhesive properties in the wet or underwater milieu is a major challenge for translating ATES solutions into in vivo applications. Water molecules form a boundary and obstruct the interactions of the moieties and chains between the adherend and the scaffold construct.[72] In the case of embedded printed HAMA-Dopa/GelMA constructs, the scaffolds were already crosslinked prior to their attachment to the collagen sheet, and therefore, small (micro) openings existed at the interface between the uneven surface of the adherend and the scaffold.[72]

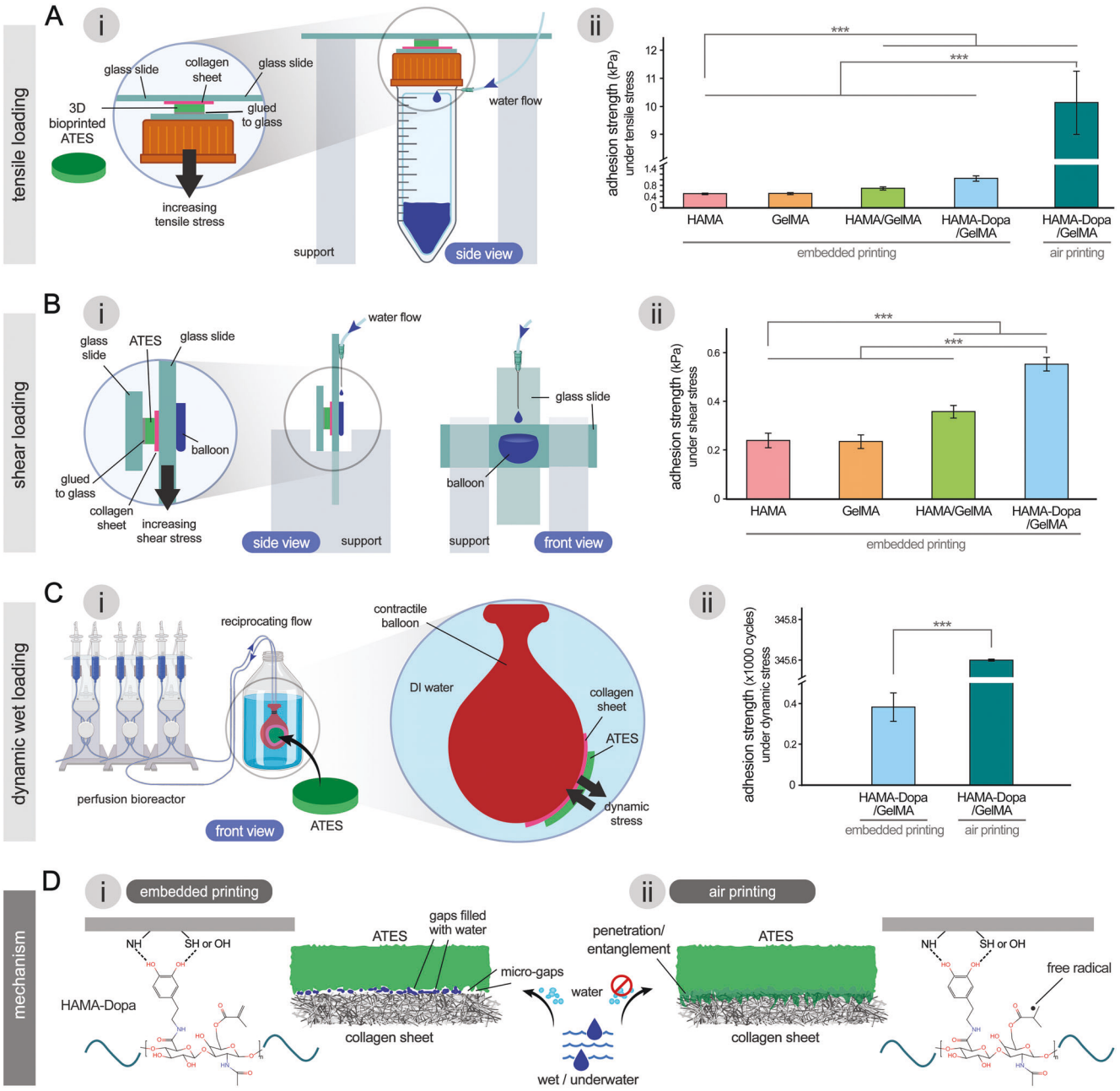

Figure 4. Evaluation of adhesive properties of the bioprinted adhesive tissue engineering scaffolds (ATESs) under various loading conditions. A-i,ii) Measuring ATES adhesive strength under steadily increasing tensile stress by uniform injection of water into a Falcone tube. A-i) Schematic illustration of the experimental set-up. A peristaltic pump was used for the controlled injection of water. The bioprinted adhesive tissue engineering scaffold (ATES) was sandwiched between a collagen sheet and two glass slides, located on top of the tube. A-ii) Quantified adhesion strength under tensile stress for methacrylated hyaluronic acid (HAMA), gelatin methacrylate (GelMA), HAMA/GelMA, and dopamine-modified HAMA (HAMA-Dopa)/GelMA printed via embedded technique, and HAMA-Dopa/GelMA via air printing ($n = 4$). B-i,ii) Evaluating adhesion under steadily increasing shear stress. B-i) Schematic illustration of experimental set-up. A peristaltic pump was used for uniform injection of water into a balloon attached to the outer side of the glass slide. ATES was sandwiched between a collagen sheet and two glass slides. B-ii) Quantified adhesion strength under shear for HAMA, GelMA, HAMA/GelMA, and HAMA-Dopa/GelMA printed via embedded technique ($n = 4$). The HAMA-air-printed Dopa/GelMA group did not break adhesion and is not presented. C-i,ii) Evaluating adhesion under wet dynamic loading conditions. C-i) Schematic illustration of experimental set-up. ATES constructs were adhered (naturally) onto the collagen sheet that was attached (glued) to the surface of contracting balloon (60 BPM, via a pump), while immersed in the water. C-ii) Quantified adhesion strength under dynamic stress for embedded and air printed HAMA-Dopa/GelMA scaffolds ($n = 3$). Other experimental groups did not tolerate the loading conditions and are not presented. Data are represented as mean ± standard deviation. *: $p < 0.05$, **: $p < 0.01$, and ***: $p < 0.001$. D) The adhesion mechanism of ATESs created via i) embedded bioprinting versus ii) air bioprinting method. The micro gaps at the ATES-substrate interface are filled with deionized (DI) water in embedded prints (underwater), while the air prints penetrate deep into the porous substrate and create stronger bonds.

Also, due to the solid, fully cured state of the hydrogel, effective penetration/entanglement of polymer chains into the surface of the adherend were limited. As a result, in the embedded printed group, water molecules would permeate through the gaps and more effectively obstruct the adhesion between the ATES and the adherend (Figure 4D-i). These are while, the semi-liquid air-printed hydrogel could effectively interact with and penetrate into the collagen substrate, leaving significantly lower level of micro-gaps at the interface; hence, higher wet adhesion strength was obtained (Figure 4D-ii). Due to poor adhesive properties, HAMA and GelMA constructs were not able to tolerate these dynamic contractions and failed instantly; hence, these groups are not presented in the data for the last set of experiments (Figure 4C).

Mechanical properties (e.g., elastic modulus or stiffness) of 3D bioprinted scaffolds are among the key characteristics of these constructs that significantly impact their biological function.[73–75] Printed tissue stiffness directly influences the cell behavior within the 3D space (e.g., differentiation, proliferation, and migration), the biomechanical coupling of implanted scaffold with the host tissue (e.g., integration with the host myocardium), its biodegradation, and several other processes.[74] In this study, while the main focus was on developing and improving adhesive properties of bioprinted scaffolds, we monitored the resulting stiffness of ATES constructs to ensure that they are within the appropriate range, approaching those in the various native soft tissues (e.g., human myocardium and vascular tissues) (**Figure 5**; Figure S2, Supporting Information).[76,77] The Young's modulus of the ATESs was measured at 17.3 ± 1.0, 15.3 ± 1.4, 21.0 ± 2.5, and 22.7 ± 3.1 kPa, for bioprinted HAMA, GelMA, HAMA/GelMA, and HAMA-Dopa/GelMA groups, respectively (Figure 5E).

Of note, the hybrid hydrogel groups, that is, HAMA/GelMA and HAMA Dopa/GelMA groups, demonstrated significantly greater moduli and stiffness values ($p < 0.05$, 0.01, and 0.001) in comparison to single hydrogel groups (HAMA and GelMA) (Figure 5E; Figure S2E, Supporting Information). These increases could be explained by the increased total polymer concentration and crosslink density in the hybrid groups. The increased levels of Young's modulus for HAMA-dopa/GelMA group can be attributed to the chelation formed between the dopamine groups of HAMA-Dopa and the amine or hydroxyl groups from the backbone of HA and gelatin, which can in turn increase the crosslink density of the ATES. Overall, the bioprinted ATES constructs demonstrated elastic moduli ranging from 14 to 25 kPa which is well in line with the modulus reported for soft tissues in the human body.[76,78] Broader ranges of elastic moduli/stiffness may be accessible from these ATES systems through further tuning of the polymers concentration, as well as adjusting the photocrosslinking parameters (e.g., UV exposure duration and intensity[23,73]).

We also examined the stability of the printed scaffolds after incubation in PBS, examining their wet weight at multiple time points (normalized to the weight at day 0 as baseline) (Figure 5F). Weight measurements of the ATESs at days 3 and 7 showed relative stability of constructs and only small weight losses for various groups. The HAMA group showed the reduction of weight by the largest margin, measuring at 84.4 ± 2.6% on day 3, and 78.6 ± 2.8% on the day 7. This reduction may be explained by the small release of the residual Carbopol particles from the construct and/or the removal of non-crosslinked free polymers.[23,79] All other groups (GelMA, HAMA/GelMA, and HAMA-Dopa/GelMA) showed comparable levels of swelling ratios, which were higher than those for the HAMA group, and showed negligible changes over the 7-day of incubation period, suggesting minimal swelling and/or degradation of bioprinted constructs (Figure 5F). Of note, the addition of GelMA to the bioinks resulted is smaller weight loss of bioprinted constructs, in comparison to the HAMA group, signifying the role of GelMA in stabilizing these ATES systems.[80,81] These results are in line with the fidelity measurements conducted on both embedded and air printed ATESs immersed in PBS, demonstrating rather negligible structural changes after one week of incubation (Figure 3C,D).

Achieving adequate adhesive functionality in bioprinted scaffold devices would be of significance only if their biocompatibility and bioactivity are maintained to the levels required for biomedical applications.[14,43,82] Various bioprinted ATES constructs in this study were examined for potential cytotoxic effects via both direct cell culture onto the engineered scaffolds, as well as testing the extracted media obtained from the scaffolds onto active cell cultures (**Figure 6**). Live/Dead assay results on mouse fibroblast cells cultured onto the GelMA (control) and HAMA-Dopa/GelMA constructs demonstrated relatively high levels of cell viability and growth over the in vitro culture period (Figure 6A-i,ii). On day 1, there were relatively (qualitatively) greater number of fibroblasts adhered onto the HAMA-Dopa/GelMA scaffold, compared to the GelMA control (Figure 6A-i); this could be attributed to the formation of chelation with amine or hydroxyl groups on the cells surface in the modified dopamine groups which could improve cell affinity.[27] We further conducted a quantitative CCK-8 assay on the mouse fibroblast (L929) cells cultured with the ATES-extracted media (Figure 6B). At day 1 of culture, the optical density (OD) values of experimental groups, normalized by the OD of cell culture media, were obtained at 1.5 ± 0.3, 1.4 ± 0.3, 1.2 ± 0.3, and 1.0 ± 0.0 for the HAMA, GelMA, HAMA/GelMA, and HAMA-Dopa/GelMA groups, respectively. On day 3, the ratios of 1.1 ± 0.1, 0.8 ± 0.1, 1.0 ± 0.1, and 1.1 ± 0.1 were obtained for HAMA, GelMA, HAMA/GelMA, and HAMA-Dopa/GelMA groups, respectively (Figure 6B-ii). These quantitative data showed that not only the extracted residues from all groups had no adverse effect on the ongoing cell cultures, they even improved the cell viability/growth in multiple conditions. In particular, the HAMA-Dopa/GelMA group, with the highest adhesive functionality, showed cell support properties consistent with those obtained from the pure culture media (control). Together, these results demonstrate adequate biocompatibility of bioprinted ATES constructs for biomedical applications. More in-depth and long-term characterization of the biological function of the ATES constructs would be required, in the future works, to further evaluate the capacity of these scaffoldings system for various translational applications.

4. Conclusion

This study introduced the first generation of ATES devices manufactured using embedded and air bioprinting methods. Results demonstrated critically different adhesion mechanisms when the ATES constructs are printed, crosslinked, and subsequently

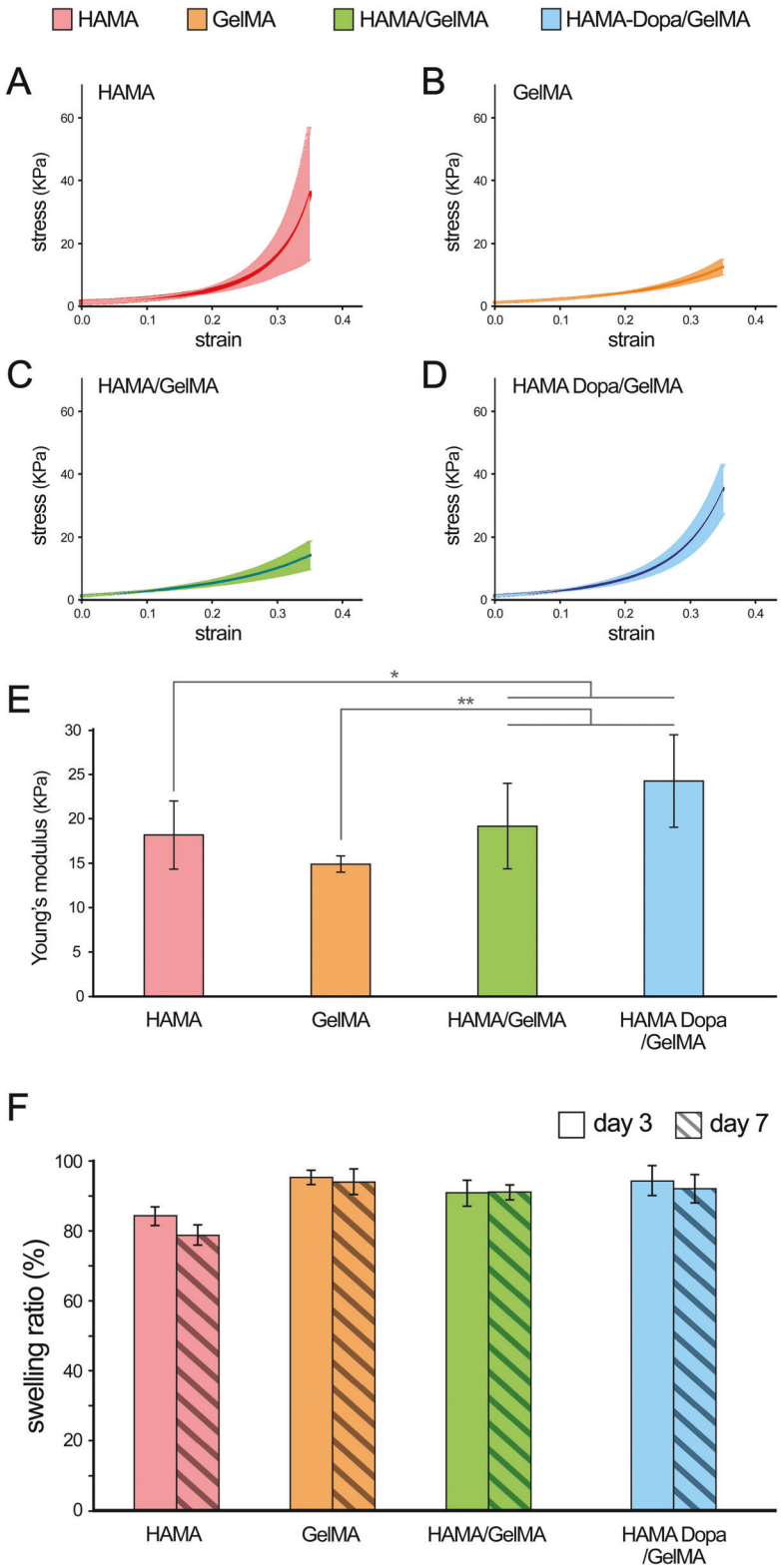

Figure 5. Evaluation of mechanical properties of the bioprinted adhesive tissue engineering scaffolds (ATESs) used in this study. A–D) Strain–stress curves of embedded 3D bioprinted methacrylated hyaluronic acid (HAMA), gelatin methacrylate (GelMA), HAMA/GelMA, and dopamine-modified HAMA (HAMA-Dopa)/GelMA scaffolds obtained from the unconfined compressive test ($n = 4$). The dark shaded region in the middle of the curve represents the average data. E) Young's modulus of ATES groups were calculated from the slope of the strain–stress curve for each group at 9–11% of displacement ($n = 4$). F) Swelling behavior of ATES measured at days 3 and 7 of incubation in PBS ($n = 4$). Data are represented as mean ± standard deviation. *: $p < 0.05$, **: $p < 0.01$, and ***: $p < 0.001$.

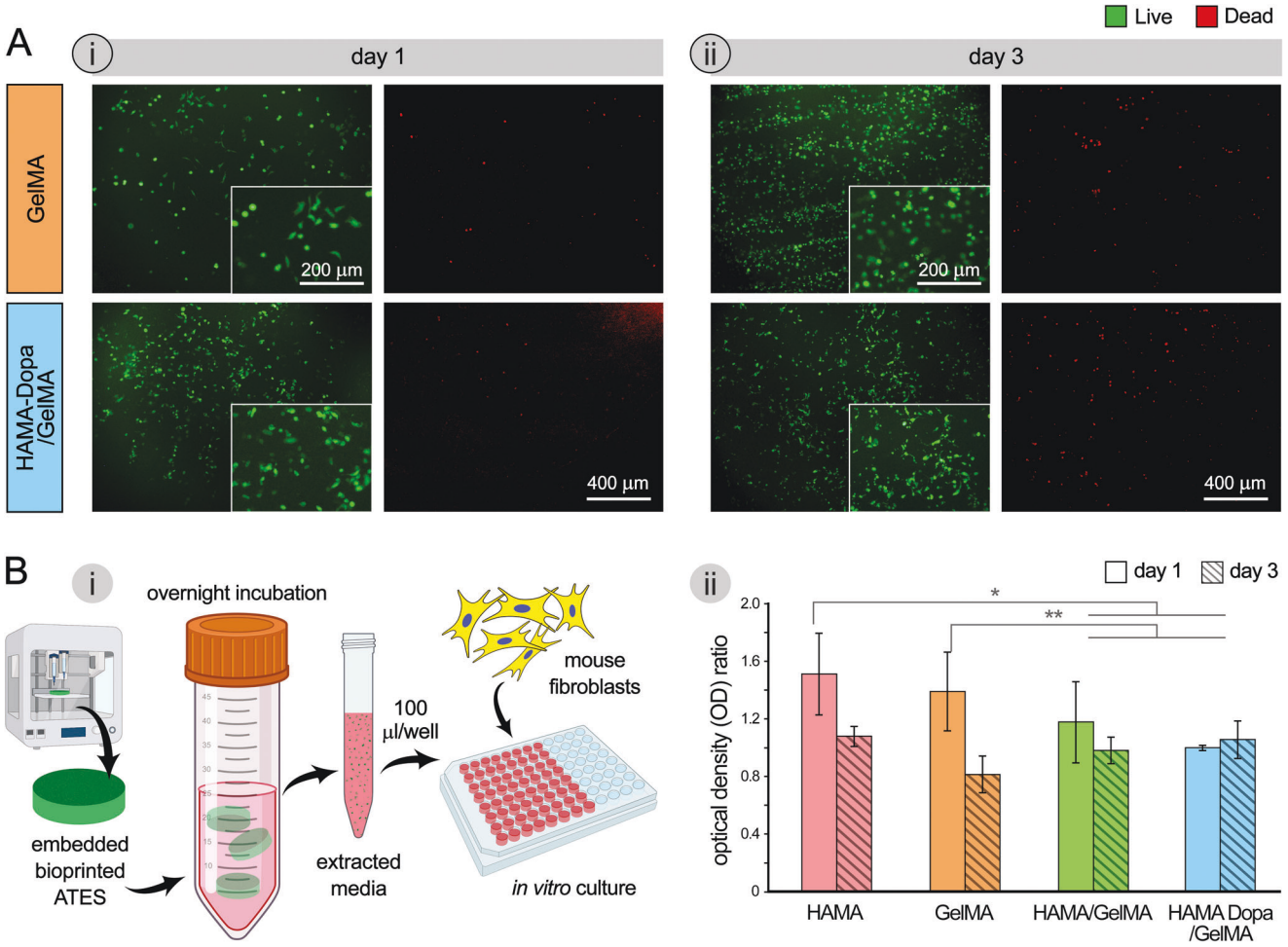

Figure 6. Evaluation of biocompatibility of the bioprinted adhesive tissue engineering scaffolds (ATESs). A) Live/Dead staining results for L929 mouse fibroblasts cultured onto embedded bioprinted GelMA (control) and HAMA-Dopa/GelMA constructs (5×10^5 cells mL^{-1}) at i) day 1 and ii) day 3 of culture. Insets in microscopy images provide higher-magnification of the live cell staining at each time point. B-i) Schematic illustration of the experimental steps used to collect ATES-conditioned media (extracted media) from GelMA (control) and HAMA-Dopa/GelMA constructs, which was subsequently used to culture L929 fibroblasts. B-ii) Quantitative cell counting kit (CCK-8) assay results for fibroblast viability obtained from in vitro culture with the extracted media prepared in (i) ($n = 4$). Optical density (OD) value of each scaffold group was normalized by the OD value obtained from cells cultured with pure culture media (control) at each time point. Data are represented as mean ± standard deviation. *: $p < 0.05$, **: $p < 0.01$, and ***: $p < 0.001$.

transferred onto the target tissue (i.e., the embedded approach) versus when directly printed and crosslinked onto the target tissue (i.e., the air or in situ printing). This major difference in the adhesive mechanism would be of great significance in the future clinical translation of bioprinted products. For embedded bioprints, the strong adhesion properties were mainly achieved by the chelation formed by dopamine molecules modified to the backbone of the HAMA and the hydroxyl and amino groups on the adherend surface. In air-printed ATESs, adhesive strength was mainly achieved by the chelation of dopamine as well as the reaction between the initiated radicals from methacrylate group on the scaffold and the moieties on the substrate. In addition, the semi liquid state of the bioink, extruded directly onto the adherend in the air printing approach results in partial penetration and integration/entanglement of the polymer molecules into the substrate, which in turn enhanced the adhesive properties. On the contrary, embedded ATES constructs that are transferred to the host tissue post crosslinking may create micro cavities at the uneven interface with the adherend and deteriorate the adhesive properties, particularly under the wet conditions. Overall, the bioprinted HAMA-Dopa/GelMA scaffolds demonstrated adequate levels of printing fidelity, structural stability, mechanical properties, biocompatibility, and adhesive strengths under varying biologically relevant loading conditions, particularly under the wet dynamic loading. The embedded printed ATESs may be considered as off-the-shelf medical device products for clinical applications, while the air-printed scaffolds need to be directly extruded onto the host tissue surface to achieve the maximal adhesion strength. This could further complicate the surgical delivery/application of air-printed ATESs for the clinical applications. In the future, design and fabrication of bioprinted ATES solutions with further enhanced adhesive properties that could fulfil long-term physiological function under harsh/dynamic loading conditions would be of great importance. More in-depth and

comprehensive biological assays would be also needed to characterize and optimize the cell-biomaterial interactions in the bioprinted ATES systems toward diverse clinical applications. Finally, more complex tissue geometries, such as interconnected vascular networks or patient-specific heterogenous tissue architectures, could be incorporated into the bioprinted ATES devices to further enhance their biomedical functions.

Supporting Information

Supporting Information is available from the Wiley Online Library or from the author.

Conflict of Interest

The authors declare no conflict of interest.

Data Availability Statement

The data that support the findings of this study are available from the corresponding author upon reasonable request.

Keywords

3D bioprinting, adhesion properties, adhesive tissue engineering scaffolds, dopamine-modified methacrylated hyaluronic acid, gelatin methacrylate

Received: March 22, 2023
Revised: April 15, 2023
Published online: May 2, 2023

[1] L. Ge, S. Chen, *Polymers* **2020**, *12*, 939.
[2] S. Nam, D. Mooney, *Chem. Rev.* **2021**, *121*, 11336.
[3] G. Pascual, S. Sotomayor, M. Rodriguez, B. Pérez-Köhler, A. Kühnhardt, M. Fernandez-Gutierrez, J. San Román, J. M. Bellón, *PLoS One* **2016**, *11*, e0157920.
[4] W. D. Spotnitz, International Scholarly Research Notices. 2014, **2014**.
[5] A. Lauto, D. Mawad, L. J. R. Foster, *J. Chem. Technol. Biotechnol.* **2008**, *83*, 464.
[6] S. Burks, W. Spotnitz, *AORN J.* **2014**, *100*, 160.
[7] V. Bhagat, M. L. Becker, *Biomacromolecules* **2017**, *18*, 3009.
[8] M. Malki, S. Fleischer, A. Shapira, T. Dvir, *Nano Lett.* **2018**, *18*, 4069.
[9] T. Vermonden, N. E. Fedorovich, D. van Geemen, J. Alblas, C. F. van Nostrum, W. J. Dhert, W. E. Hennink, *Biomacromolecules* **2008**, *9*, 919.
[10] C. Wiltsey, T. Christiani, J. Williams, J. Scaramazza, C. Van Sciver, K. Toomer, J. Sheehan, A. Branda, A. Nitzl, E. England, *Acta Biomater.* **2015**, *16*, 71.
[11] M. Ark, P. Boughton, A. Lauto, G. T. Tran, Y. Chen, P. H. Cosman, C. R. Dunstan, *J. Mech. Behav. Biomed. Mater.* **2016**, *62*, 433.
[12] C. Salzlechner, T. Haghighi, I. Huebscher, A. R. Walther, S. Schell, A. Gardner, G. Undt, R. M. da Silva, C. A. Dreiss, K. Fan, *Adv. Healthcare Mater.* **2020**, *9*, 1901134.
[13] Y. Hong, F. Zhou, Y. Hua, X. Zhang, C. Ni, D. Pan, Y. Zhang, D. Jiang, L. Yang, Q. Lin, Y. Zou, D. Yu, D. E. Arnot, X. Zou, L. Zhu, S. Zhang, H. Ouyang, *Nat. Commun.* **2019**, *10*, 2060.
[14] S. Chen, C. Gil, L. Ning, L. Jin, L. Perez, G. Kabboul, M. L. Tomov, V. Serpooshan, *Front. Bioeng. Biotechnol.* **2021**, *9*, 673240.
[15] S. V. Murphy, A. Atala, *Nat. Biotechnol.* **2014**, *32*, 773.
[16] Y. S. Zhang, K. Yue, J. Aleman, K. Mollazadeh-Moghaddam, S. M. Bakht, J. Yang, W. Jia, V. Dell'Erba, P. Assawes, S. R. Shin, *Ann. Biomed. Eng.* **2017**, *45*, 148.
[17] J. B. Hu, M. L. Tomov, J. W. Buikema, C. Chen, M. Mahmoudi, S. M. Wu, V. Serpooshan, *Appl. Phys. Rev.* **2018**, *5*, 041106.
[18] P. Rider, Z. P. Kacarevic, S. Alkildani, S. Retnasingh, M. Barbeck, *J. Tissue Eng.* **2018**, *9*, 204173141880209.
[19] G. Gillispie, P. Prim, J. Copus, J. Fisher, A. G. Mikos, J. J. Yoo, A. Atala, S. J. Lee, *Biofabrication* **2020**, *12*, 022003.
[20] F. You, B. F. Eames, X. Chen, *Int. J. Mol. Sci.* **2017**, *18*, 1597.
[21] M. Hospodiuk, K. K. Moncal, M. Dey, I. T. Ozbolat, in *3D Printing and Biofabrication*, Vol. *1* (Eds: A. Ovsianikov, J. Yoo, V. Mironov), Springer International Publishing, Cham **2018**, p. 12.
[22] I. T. Ozbolat, M. Hospodiuk, *Biomaterials* **2016**, *76*, 321.
[23] L. Ning, R. Mehta, C. Cao, A. Theus, M. Tomov, N. Zhu, E. R. Weeks, H. Bauser-Heaton, V. Serpooshan, *ACS Appl. Mater. Interfaces* **2020**, *12*, 44563.
[24] E. Mirdamadi, J. W. Tashman, D. J. Shiwarski, R. N. Palchesko, A. W. Feinberg, *ACS Biomater. Sci. Eng.* **2020**, *6*, 6453.
[25] D. J. Shiwarski, A. R. Hudson, J. W. Tashman, A. W. Feinberg, *APL Bioeng.* **2021**, *5*, 010904.
[26] T. J. Hinton, Q. Jallerat, R. N. Palchesko, J. H. Park, M. S. Grodzicki, H.-J. Shue, M. H. Ramadan, A. R. Hudson, A. W. Feinberg, *Sci. Adv.* **2015**, *1*, e1500758.
[27] L. Han, M. Wang, P. Li, D. Gan, L. Yan, J. Xu, K. Wang, L. Fang, C. W. Chan, H. Zhang, *ACS Appl. Mater. Interfaces* **2018**, *10*, 28015.
[28] S. K. Seidlits, Z. Z. Khaing, R. R. Petersen, J. D. Nickels, J. E. Vanscoy, J. B. Shear, C. E. Schmidt, *Biomaterials* **2010**, *31*, 3930.
[29] E. Shirzaei Sani, A. Kheirkhah, D. Rana, Z. Sun, W. Foulsham, A. Sheikhi, A. Khademhosseini, R. Dana, N. Annabi, *Sci. Adv.* **2019**, *5*, eaav1281.
[30] A. S. Theus, L. Ning, G. Kabboul, B. Hwang, M. L. Tomov, C. N. LaRock, H. Bauser-Heaton, M. Mahmoudi, V. Serpooshan, *iScience* **2022**, *25*, 104947.
[31] L. Ning, J. Shim, M. L. Tomov, R. Liu, R. Mehta, A. Mingee, B. Hwang, L. Jin, A. Mantalaris, C. Xu, M. Mahmoudi, K. C. Goldsmith, V. Serpooshan, *Adv. Sci.* **2022**, *9*, 2200244.
[32] M. L. Tomov, L. Perez, L. Ning, H. Chen, B. Jing, A. Mingee, S. Ibrahim, A. S. Theus, G. Kabboul, K. Do, S. R. Bhamidipati, J. Fischbach, K. McCoy, B. A. Zambrano, J. Zhang, R. Avazmohammadi, A. Mantalaris, B. D. Lindsey, D. Frakes, L. P. Dasi, V. Serpooshan, H. Bauser-Heaton, *Adv. Healthcare Mater.* **2022**, *11*, 2201227.
[33] Y. P. Yu, B. H. Kwan, C. L. Lim, S. L. Wong, P. Raveendran, in *2013 International Symposium on Intelligent Signal Processing and Communication Systems*, IEEE, Naha, Japan, **2013**.
[34] S. E. Koch, E. E. van Haaften, T. B. Wissing, L. A. B. Cuypers, J. A. Bulsink, C. V. C. Bouten, N. A. Kurniawan, A. Smits, *J. Vis. Exp.* **2020**, *166*, 347.
[35] M. G. Drozdova, D. S. Zaytseva-Zotova, R. A. Akasov, A. S. Golunova, A. A. Artyukhov, O. O. Udartseva, E. R. Andreeva, D. E. Lisovyy, M. I. Shtilman, E. A. Markvicheva, *Mater. Sci. Eng., C* **2017**, *75*, 1075.
[36] W. Gao, H. Chao, Y.-C. Zheng, W.-C. Zhang, J. Liu, F. Jin, X.-Z. Dong, Y.-H. Liu, S.-J. Li, M.-L. Zheng, *ACS Appl. Mater. Interfaces* **2021**, *13*, 27796.
[37] L. Cai, X. Qin, Z. Xu, Y. Song, H. Jiang, Y. Wu, H. Ruan, J. Chen, *ACS Omega* **2019**, *4*, 12036.
[38] J. Zhang, X. Ma, D. Fan, C. Zhu, J. Deng, J. Hui, P. Ma, *Mater. Sci. Eng., C* **2014**, *43*, 547.
[39] X. Zhang, G.-h. Sun, M.-p. Tian, Y.-n. Wang, C.-c. Qu, X.-j. Cheng, C. Feng, X.-g. Chen, *Int. J. Biol. Macromol.* **2019**, *138*, 321.
[40] W. D. Spotnitz, *ISRN Surg.* **2014**, 203943. https://doi.org/10.1016/j.mtbio.2023.100599

[41] G. Pascual, S. Sotomayor, M. Rodriguez, B. Perez-Kohler, A. Kuhnhardt, M. Fernandez-Gutierrez, J. S. Roman, J. M. Bellon, *PLoS One* **2016**, *11*, e0157920.
[42] W. Furst, A. Banerjee, *Ann. Thorac. Surg.* **2005**, *79*, 1522.
[43] C. S. Russell, A. Mostafavi, J. P. Quint, A. C. Panayi, K. Baldino, T. J. Williams, J. G. Daubendiek, V. H. Sanchez, Z. Bonick, M. Trujillo-Miranda, S. R. Shin, O. Pourquie, S. Salehi, I. Sinha, A. Tamayol, *ACS Appl. Bio. Mater.* **2020**, *3*, 1568.
[44] S. Chen, C. J. Gil, L. Ning, L. Jin, L. Perez, G. Kabboul, M. L. Tomov, V. Serpooshan, *Front. Bioeng. Biotechnol.* **2021**, *9*, 683079.
[45] Y. Zhou, J. Zhao, X. Sun, S. Li, X. Hou, X. Yuan, X. Yuan, *Biomacromolecules* **2016**, *17*, 622.
[46] B. Saleh, H. K. Dhaliwal, R. Portillo-Lara, E. Shirzaei Sani, R. Abdi, M. M. Amiji, N. Annabi, *Small* **2019**, *15*, 1902232.
[47] K. Lei, Q. Zhu, X. Wang, H. Xiao, Z. Zheng, *ACS Biomater. Sci. Eng.* **2019**, *5*, 5489.
[48] L. Koivusalo, M. Kauppila, S. Samanta, V. S. Parihar, T. Ilmarinen, S. Miettinen, O. P. Oommen, H. Skottman, *Biomaterials* **2019**, *225*, 119516.
[49] B. W. Walker, R. P. Lara, C. H. Yu, E. S. Sani, W. Kimball, S. Joyce, N. Annabi, *Biomaterials* **2019**, *207*, 89.
[50] P. Datta, B. Ayan, I. T. Ozbolat, *Acta Biomater.* **2017**, *51*, 1.
[51] B. Byambaa, N. Annabi, K. Yue, G. Trujillo-de Santiago, M. M. Alvarez, W. Jia, M. Kazemzadeh-Narbat, S. R. Shin, A. Tamayol, A. Khademhosseini, *Adv. Healthcare Mater.* **2017**, *6*, 1700015.
[52] A. A. De la Lastra, K. R. Hixon, L. Aryan, A. N. Banks, A. Y. Lin, A. F. Hall, S. A. Sell, *J. Funct. Biomater.* **2018**, *9*, 46.
[53] K. Hozumi, M. Nomizu, *Int. J. Mol. Sci.* **2018**, *19*, 2713.
[54] B. Sarker, J. Rompf, R. Silva, N. Lang, R. Detsch, J. Kaschta, B. Fabry, A. R. Boccaccini, *Int. J. Biol. Macromol.* **2015**, *78*, 72.
[55] T. T. Hoang Thi, Y. Lee, P. L.e Thi, K. D. Park, *J. Ind. Eng. Chem.* **2019**, *78*, 34.
[56] X. Pei, J. Wang, Y. Cong, J. Fu, *J. Polym. Sci.* **2021**, *59*, 1312.
[57] S. Chen, C. J. Gil, L. Ning, L. Jin, L. Perez, G. Kabboul, M. L. Tomov, V. Serpooshan, *Front. Bioeng. Biotechnol.* **2021**, *9*, 683079.
[58] N. Rajabi, A. Rezaei, M. Kharaziha, H. R. Bakhsheshi-Rad, H. Luo, S. RamaKrishna, F. Berto, *Tissue Eng., Part A* **2021**, *27*, 679.
[59] R. Leu Alexa, H. Iovu, J. Ghitman, A. Serafim, C. Stavarache, M. M. Marin, R. Ianchis, *Polymers* **2021**, *13*, 727.
[60] M. T. Poldervaart, B. Goversen, M. de Ruijter, A. Abbadessa, F. P. W. Melchels, F. C. Oner, W. J. A. Dhert, T. Vermonden, J. Alblas, *PLoS One* **2017**, *12*, e0177628.
[61] M. Mohammed, N. Devnarain, E. Elhassan, T. Govender, *Wiley Interdiscip. Rev. Nanomed. Nanobiotechnol.* **2022**, *14*, e1799.
[62] Z. Zhu, Y.-M. Wang, J. Yang, X.-S. Luo, *Plast. Aesthet. Res.* **2017**, *4*, 219.
[63] A. B. Bello, D. Kim, D. Kim, H. Park, S. H. Lee, *Tissue Eng., Part B Rev.* **2020**, *26*, 164.
[64] T.-D. Zhang, X. Deng, Y.-F. Wang, X.-T. Wang, X. Zhang, L.-L. Chen, X. Cao, Y.-Z. Zhang, C.-Y. Zhang, X. Zheng, *Appl. Surf. Sci.* **2020**, *530*, 147197.
[65] P. Song, M. Li, B. Zhang, X. Gui, Y. Han, L. Wang, W. Zhou, L. Guo, Z. Zhang, Z. Li, *Composites, Part B* **2022**, *244*, 110163.
[66] H. Shirahama, B. H. Lee, L. P. Tan, N.-J. Cho, *Sci. Rep.* **2016**, *6*, 31036.
[67] L. Li, C. J. Gil, T. A. Finamore, C. J. Evans, M. L. Tomov, L. Ning, A. Theus, G. Kabboul, V. Serpooshan, R. K. Roeder, *Adv. Nanobiomed. Res.* **2022**, *2*, 2200022.
[68] A. McCormack, C. B. Highley, N. R. Leslie, F. P. W. Melchels, *Trends Biotechnol.* **2020**, *38*, 584.
[69] X. Wei, Y. Luo, P. Huang, *Polym. Bull.* **2019**, *76*, 6077.
[70] Y. Yong-Ze, Z. Lu-Lu, C. Hai-Ping, C. Wei-Hua, H. Qing-Xi, *Adv. Manuf.* **2014**, *2*, 231.
[71] Y. Chen, H. Qin, A. Mensaha, Q. Wang, F. Huang, Q. Wei, *Composites, Part B* **2021**, *222*, 109071.
[72] H. Y. Yuen, H. P. Bei, X. Zhao, *Chem. Eng. J.* **2022**, *431*, 133372.
[73] L. Ning, C. J. Gil, B. Hwang, A. S. Theus, L. Perez, M. L. Tomov, H. Bauser-Heaton, V. Serpooshan, *Appl. Phys. Rev.* **2020**, *7*, 041319.
[74] R. G. Breuls, T. U. Jiya, T. H. Smit, *Open Orthop. J.* **2008**, *2*, 103.
[75] N. Sultana, in *Functional 3D Tissue Engineering Scaffolds* (Eds: Y. Deng, J. Kuiper), Woodhead Publishing, Cambridge **2018**, p. 1
[76] M.-H. Lu, R. Mao, Y. Lu, Z. Liu, T.-F. Wang, S.-P. Chen, *Comput. Math. Methods. Med.* **2012**, 979847. https://doi.org/10.1155/2012/979847
[77] K. Hayashi, in *Biomechanics of Soft Tissue in Cardiovascular Systems* (Eds: G. A. Holzapfel, R. W. Ogden), Springer Vienna, Vienna **2003**, Ch. *2*. p. 441
[78] R. Akhtar, M. J. Sherratt, J. K. Cruickshank, B. Derby, *Mater. Today* **2011**, *14*, 96.
[79] S. M. Bittner, H. A. Pearce, K. J. Hogan, M. M. Smoak, J. L. Guo, A. J. Melchiorri, D. W. Scott, A. G. Mikos, *Tissue Eng., Part A* **2021**, *27*, 665.
[80] M. Y. Shie, J. J. Lee, C. C. Ho, S. Y. Yen, H. Y. Ng, Y. W. Chen, *Polymers* **2020**, *12*, 1930.
[81] M. Sun, X. Sun, Z. Wang, S. Guo, G. Yu, H. Yang, *Polymers* **2018**, *10*, 1290.
[82] S. Chen, M. Tomov, L. Ning, C. Gil, B. Hwang, H. Bauser-Heaton, V. Serpooshan, *Circ. Res.* **2021**, *129*, 403.

